

The Enigmatic Smooth Patch on Comet 9P/Tempel 1: Revisiting Deep Impact and Stardust/NExT Missions Outcomes for Novel Perspectives

J. L. Rizos^{1,2}, T. L. Farnham¹, J. Kloos¹, J. M. Sunshine¹, J. L. Ortiz²

1 - University of Maryland, MD – USA (jlrizos@iaa.es)

2 - Instituto de Astrofísica de Andalucía, Spain

Abstract

We present a comprehensive analysis of the region containing the large smooth patch on comet Tempel 1, focusing on its spectral and morphological characteristics and those of its surroundings. Utilizing observational data from the Deep Impact and Stardust-NExT missions, an updated stereophotoclinometry-based shape model, and numerical simulations, we aim to investigate the origin and evolution of this feature. Our study characterizes the morphological changes between the two mission visits, determining that the smooth patch has a thickness of approximately 25 meters. This patch is embedded in a cliff with an average height of 50 meters and exhibits a lobate U-shape morphology. Our findings support the previously suggested idea that an ice flow phenomenon is compatible with the observations. Moreover, our simulations indicate that a single phenomenon could link both the large and secondary smooth patches and the mass wasting feature observed on the comet's opposite northern face. We propose that a cryovolcano-like event may be responsible for this smooth feature, although more evidence is needed to support this hypothesis.

1. Introduction

Comets are among the most pristine bodies in the Solar System, formed in the outermost regions of the solar nebula. Unlike main-belt asteroids or terrestrial planets, comets contain volatiles, notably water ice, which were in a solid state in the cold outer region of the solar system ([Weidenschilling 2004](#)). There exist two primary classifications of comets: long-period comets, characterized by highly eccentric orbits and orbital periods spanning from 200 to thousands of years, believed to originate from the Oort Cloud; and short-period comets, with orbital periods shorter than 200 years, thought to arise either from objects in the trans-Neptunian belt (TNB) or centaurs that have undergone interactions with giant planets, causing them to adopt orbits that traverse into the inner solar system ([Rickman 2004](#)).

Within the short-period comets, there is a special type known as Jupiter-family comets (JFCs), characterized by orbital periods shorter than 20 years and inclinations below 30 degrees. Most JFCs are

believed to originate from the Scattered Disk of the TNB ([Duncan 2008](#)). Their orbits are chaotic due to intense interaction with Jupiter, hence their name. The majority of observed JFCs likely stem from collisions within the trans-Neptunian belt (TNB) ([Stern 1995](#); [Farinella & Davis 1996](#)), and therefore, they may not accurately represent the original state of the smallest, kilometer-sized objects beyond Neptune. Nevertheless, being descendants, JFCs provide a unique dataset for understanding their ancestors and the Solar System's evolutionary processes.

Due to their short orbital periods, JFCs regularly approach the Sun, offering favorable circumstances for observation. As of now, spacecraft have visited nine JFCs: 21P/Giacobini–Zinner, 1P/Halley, 26P/Grigg–Skjellerup, 19P/Borrelly, 81P/Wild, 9P/Tempel 1, 103P/Hartley, and 67P/Churyumov–Gerasimenko. Resolved images have been captured from the latter five.

Comet 9P/Tempel 1 (T1), with an approximate diameter of ~ 6 km, belongs to the JFCs category ($q=1.5$, $Q=4.7$, $i=10.4^\circ$) and was first discovered in 1867. It was initially visited by the Deep Impact mission in 2005 ([A'Hearn et al., 2005a](#)), followed by the Stardust/NEXT mission in 2011 ([Veverka et al., 2013](#)). Being the only comet visited twice during separate apparitions, it presents a unique opportunity to document surface changes and investigate its physical properties and evolution over its complete orbital period of 5.56 years.

The Deep Impact (DI) mission, which successfully directed a 366 kg impactor-spacecraft to collide with the surface of T1 at a velocity of $10.2 \text{ km}\cdot\text{s}^{-1}$ ([A'Hearn et al., 2005b](#)), was equipped with four scientific instruments: three digital cameras —the High-Resolution Instrument (HRI), Medium Resolution Instrument (MRI), and Impactor Targeting Sensor (ITS)— and one infrared (IR) imaging spectrometer that used as its fore optics the same telescope as the HRI ([Klaasen et al., 2008](#)). On the other hand, the Stardust/NEXT (SDN) spacecraft, during its extended mission to encounter T1, carried a payload comprising three scientific instruments: a visible camera (NavCam) and two dust detection instruments ([Klaasen et al., 2013b](#)). Images of T1 captured by both spacecraft covered approximately 70% of its surface area ([Thomas et al., 2013](#)), unveiling a morphologically diverse body characterized by rough, pitted terrain and, notably, regions of smooth terrain that stand out from their surroundings. Fig. 1 shows the large smooth patch, located at the T1 south pole, surrounded by rough terrain and embedded in a cliff. In this work, we refer to the region between the edge of this large smooth patch and the cliff as the cliff region.

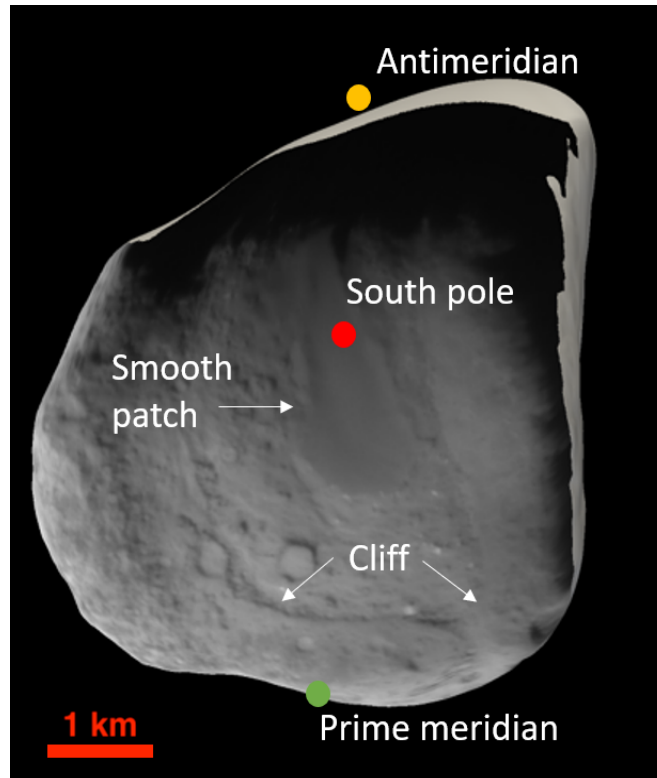


Fig. 1. 30036 SDN image projected on a shape model showing T1 south face. The low albedo smooth region in the center is the large smooth patch, surrounded by a cliff and rugged terrain. Green and blue points indicate prime meridian and antimeridian, respectively. The red point indicates the south pole.

The origins of this smooth terrain and its surrounding remains a mystery and understanding this distinctive feature could be key in deepening our comprehension of comet evolution. Since its discovery, various hypotheses have been discussed: [Belton et al., \(2007\)](#) proposed that they are primitive layers exhumed by sublimation; [Bar-Nun et al., \(2008\)](#) suggested that the smooth terrains are the result of the deposition of ice grains that were released in a collimated ejection during a massive outburst of gas; and [Belton et al., \(2009\)](#) proposed a complex subsurface fluidization production mechanism. However, none of these ideas adequately account for the observed cliff that encircles this patch. The only hypothesis, to date, capable of addressing both the large smooth patch and its outer region, suggests a material flow phenomenon ([Thomas et al., 2007](#)). Pursuing this idea, [Gougen et al., \(2008\)](#) conducted calculations estimating that the flow velocity must remain below the surface escape velocity (1.3 m/s), the material's kinematic viscosity should have exceeded $2.5 \times 10^{-3} \text{ m}^2/\text{s}$, and the flow possessed a high Reynolds number of approximately 104, indicative of turbulent flow. This aligns with the proposition by [Basilevsky and Keller \(2007\)](#), who considering improbable an eruption of materials from an active interior, suggested a sublimation-driven collapse of steep slopes and the avalanche distribution of the collapsed material within the lows.

Our goal in this work is to contribute to the ongoing discussion by reassessing previous data, capitalizing on an updated stereophotoclinometry-based shape model ([Ernst et al., 2019](#)), which offers a substantial enhancement in resolution (3,145,734 facets, with a ground sample distance of up to 8 m). For that, we investigate this large smooth patch using images from HRI, MRI, ITS, and NavCam, complemented by IR

spectral data obtained from DI. In Section 2, we present the data and methods employed in this study. In Section 3.1, a spectral data analysis from DI to identify compositional differences is shown. Additionally, in Section 3.2 we provide measurements of the thickness and extent of the large smooth patch and its surroundings using the new shape model, along with several anaglyphs that allow for the three-dimensional morphology visualization of this region. Section 3.3 offers a comparative analysis of DI and SDN images, wherein we identify and categorize morphological changes in the region. In Section 3.4, an examination of solar and thermal irradiation received over a complete orbital period is presented, followed by a numerical simulation of the hypothesized ice flow on the surface in Section 3.5. In Section 4 we discuss the most plausible explanations for the phenomenon underlying this feature compatible with the collected findings. Finally, our concluding remarks are presented in Section 5.

2. Data and methods

In this section, we introduce the dataset used in this research, as well as the analytical and numerical methodologies employed throughout this study.

2.1 Dataset

DI images: Images acquired by the DI spacecraft, stem from the HRI, MRI, and ITS instruments. Firstly, HRI comprises a Cassegrain telescope with a focal length of 10.5 m and a 30 cm aperture. It serves a dual function, feeding a filtered CCD camera (1024 x 1024 pixels) and a long-slit imaging spectrometer, separated by a dichroic beamsplitter. This beamsplitter reflects visible light (0.34 to 1.05 μm wavelength) to the CCD while transmitting IR light (1.05 to $> 4.8 \mu\text{m}$). The visible light undergoes filtration via one of nine color filters centered at 350, 450, 550, 650, 750, 850, and 950 nm, respectively. Note that HRI was discovered to be out of focus post-launch (Klaasen et al., 2008). However, there is a package of deconvolved images (Lindler et al., 2007) to enhance resolution, although they are not useful for photometric measurements due to artifacts produced by the deconvolution algorithm. Conversely, MRI and ITS, both 1024 x 1024 pixels, are similar instruments based on a 2.1 m Cassegrain telescope with a 12 cm aperture. MRI boasts nominally five times lower spatial resolution than HRI and features a nine-position filter wheel centered at 309, 345, 387, 514, 526, 650, 700, 750, or 950 nm, respectively. ITS does not filter light. The images utilized herein are accessible via the Planetary Data System (PDS¹), with information regarding their calibration and additional technical details also available in that repository.

SDN images: The images from this spacecraft were collected by the NavCam instrument. This camera, with a 0.2 m focal length, was connected to a 1024 x 1024-pixel CCD. Despite the camera's original design with various color filters, issues with the filter wheel during flight led to the availability of only images taken with the broadband optical-navigation spectral filter, which allowed light transmission from 475 to 925 nm (Klaasen et al., 2013b). Like the previous case, calibrated images used in this study have been obtained from the PDS repository.

¹ <https://pds.nasa.gov/>

Shape model: We utilize a stereophotoclinometry model of T1 as presented by [Ernest et al., \(2019\)](#), which merges DI and SDN data. In contrast to the last shape model shaped by [Farnham & Thomas \(2013\)](#), this new model enables the incorporation of local, high-level details like those observed in the images or spectra. This updated shape model, consisting of 3,145,734 facets with a ground sample distance of up to 8 meters, has been refined using 318 HRI, 379 MRI, 83 ITS, and 72 NavCam images, resulting in approximately a 20-fold enhancement in resolution compared to its predecessor.

2.2 Methods

Gravitational flow: [Thomas et al., \(2013\)](#) interpreted the large smooth patch observed in DI images as deposits resulting from flows. To examine this hypothesis, we initially computed the gravitational potential energy across the surface of T1. To achieve this, we subdivided the shape model into triangular pyramids with their apexes positioned at the origin coordinates, following the approach outlined by [Chanut et al., \(2015\)](#). To reduce computing time, the shape model is downsampled a 10% (31456 facets). We use a mean density of 400 kg/m³ ([Richardson et al., 2007](#)), an average gravity (g_r) of $2.7 \cdot 10^{-7}$ km/s² ([Thomas et al., 2007](#)) and assume a homogeneous distribution of mass. The rotational period of T1, approximately 40 hours ([Belton et al., 2011](#)) induces negligible additional acceleration on the surface gravity field ([Thomas et al., 2013](#)), hence it was disregarded.

The initial step of the simulation involves placing a seed at a point on the surface, assuming that point to be a source from which a flow originates. Subsequently, we compare the gravitational potential value of this source with that of neighboring facets. If a neighboring facet presents a lower value, the flow will occupy this facet in the next step. We iterate this algorithm until no new facets remain to be occupied. Consequently, this simulation assumes a flow with no inertia. To thoroughly explore all potential configurations, we partition the entire surface into a 200 m grid and systematically place seeds.

Rather than employing units of gravitational potential energy, which can be challenging to intuitively relate to height in a shape as irregular as T1, we opt to transform the gravitational potential (W_i) for the i -th facet into dynamic height, denoted as $D_i = \frac{W_i - W_0}{g_r}$, where W_0 represents the lowest gravitational potential energy observed on the surface ([Thomas et al., 1993](#)). Results are shown in Section X.

Solar irradiance and self-heating effects: We compute the incoming solar radiation (E_j) received by T1 in a complete orbit at each facet, j using SPICE T1 ephemerides. This is determined by considering the slope angle and orientation of the surface through a simple relationship:

$$E_j = \frac{(1 - A)\tau F_0 \left(-(\vec{s} \cdot \vec{n}_j) \right)}{d^2} = \frac{(1 - A)\tau F_0 \cos(i_j)}{d^2} \quad (1)$$

Where A represents surface albedo, τ is a binary shadowing term, F_0 denotes solar flux at 1 AU, \vec{s} is the solar vector relative to a comet-fixed reference frame, \vec{n}_j is the surface normal vector, d indicates the

comet-Sun distance in AU, and i_j is the angle of incidence of light on the surface, relative to the surface normal. Shadowing and self-heating effects are accounted for using a ray-tracing algorithm. For more details see [Kloos et al., \(2024\)](#).

3D morphologic measurements: To capture three-dimensional data of this area, we'll employ anaglyphs and photogrammetry techniques alongside the shape model.

An anaglyph comprises a pair of images (stereo-images) taken from slightly divergent viewpoints. We seek out a pair of images with comparable resolution but distinct viewing angles. Next, we adjust the RGB channels to generate red and cyan color images. Subsequently, we rotate them so the between both images seems horizontal as perceived by the observer, and gradually apply an offset until the desired 3D effect is achieved when viewed through red-cyan glasses.

On the other hand, as the shape model fails to accurately represent the elevation of the large smooth patch relative to the surrounding terrain—nevertheless it does accurately depict the heights of the cliff and spit craters—we employ a photogrammetry technique on the ITS images. We want to determine the thickness of the large smooth patch in relation to the outer area filled with pitted terrains, and the morphology of its surface. To achieve this, we take advantage of several ITS images with different emission angles where the edges are resolved (see Fig. 2a) and of the shadows cast by the central depressions (see Fig. 2b) in SDN images.

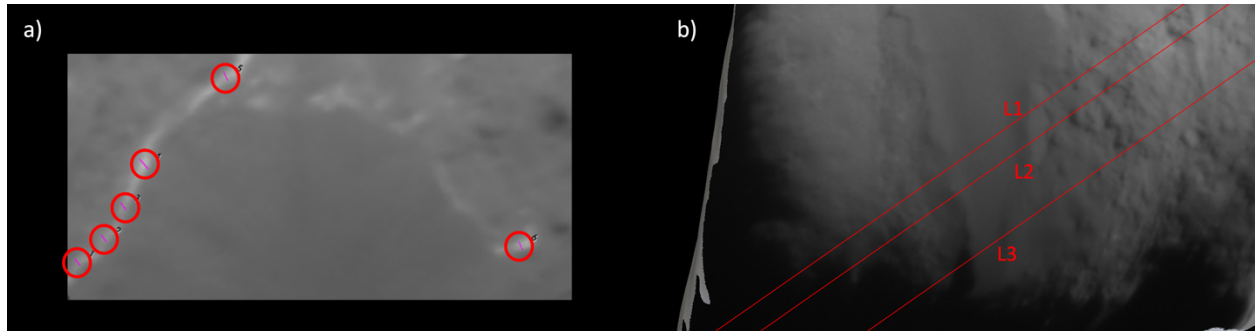


Fig. 2. a) Example of an ITS image showing the edges of the large smooth patch as seen from the camera. The red circles represents multiple measurements taken along the entire edge. b) Example of an SDN image in which shadows caused by the convex shape of the smooth patch are visible. The red lines go in the direction of the Sun and are used to measure the length of the shadows.

For a convex surface, we can establish a trigonometric relationship between the length of the shadows (L), the incidence angle at the shadow's edge (i), and the relative elevation of the endpoint (h) as $h \sim L \tan(90 - i)$ (see Fig. 3a). Also, it is possible to obtain an order of magnitude of the thickness. Considering that the projected length of an edge as seen from the camera is $S_{proj} = S \cos(e)$, where e represents the emission angle, and using the trigonometric relationship of $h = S \sin(\alpha)$ (see Fig. 3b), for non-extreme cases in when $e \approx \alpha$, the relationship $h = S_{proj} \tan(e)$ allows us to estimate the order of magnitude of the thickness of the large smooth patch. We validate this method by defining several control points (high enough to be well-defined in the shape model) and confirming that the measurements are coincident.

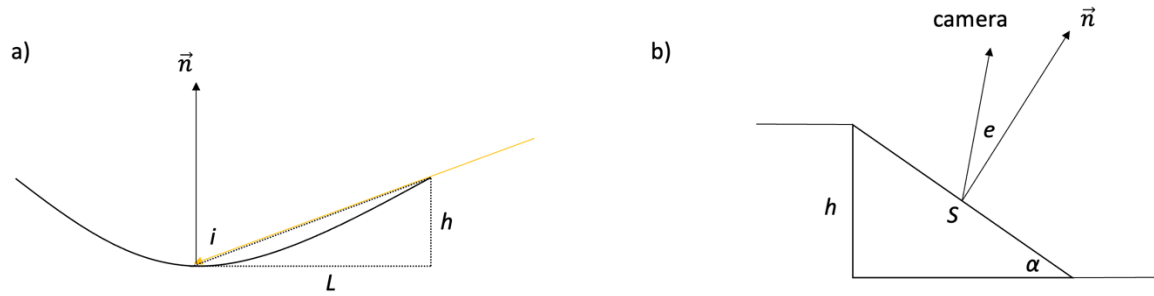


Fig. 3. a) Diagram showing the smooth patch surface as seen by NavCam where we establish a relationship between the relative elevation of the endpoint (h), the incidence angle (i), and the length of the shadow (L). **b)** Diagram of the smooth patch edge seen by ITS. The emission angle (e) and the edge length (S) can be related to get the order of magnitude of the thickness (h).

Results

In this section, we present the results of the analyses carried out. First, we used spectral data from DI to study if there are evident compositional differences between the large smooth patch and the rest of the surface; the results are presented in Section 3.1. In Section 3.2, we show the outcomes of direct measurements of thickness and morphology using the programming techniques developed in the previous section, as well as through direct measurements on the shape model. In Section 3.3, we perform a visual comparison between the images taken by DI and those by SDN to identify and group changes on the surface between the two visits to T1. Section 3.4 shows the results of solar and thermal self-irradiation modeling, and finally, in Section 3.5, the results of an ice-flow simulation are presented.

3.1 Spectral data

Using the 350, 450, 550, 650, 750, 850, and 950 nm color filters of HRI, we get the spectra in the visible range from four distinct regions of T1 (refer to Fig. 4). Region 1 specifically targets an area within the large smooth patch. To facilitate comparison, we normalized the values at 650 nm. The error is the standard deviation of each square. This process was repeated for the IR spectra, which were normalized at 2 microns. All spectra were obtained at a phase angle of 62.9° . Interestingly, no significant spectral disparities were observed in any case, indicating that the composition of the four regions exhibits no measurable differences.

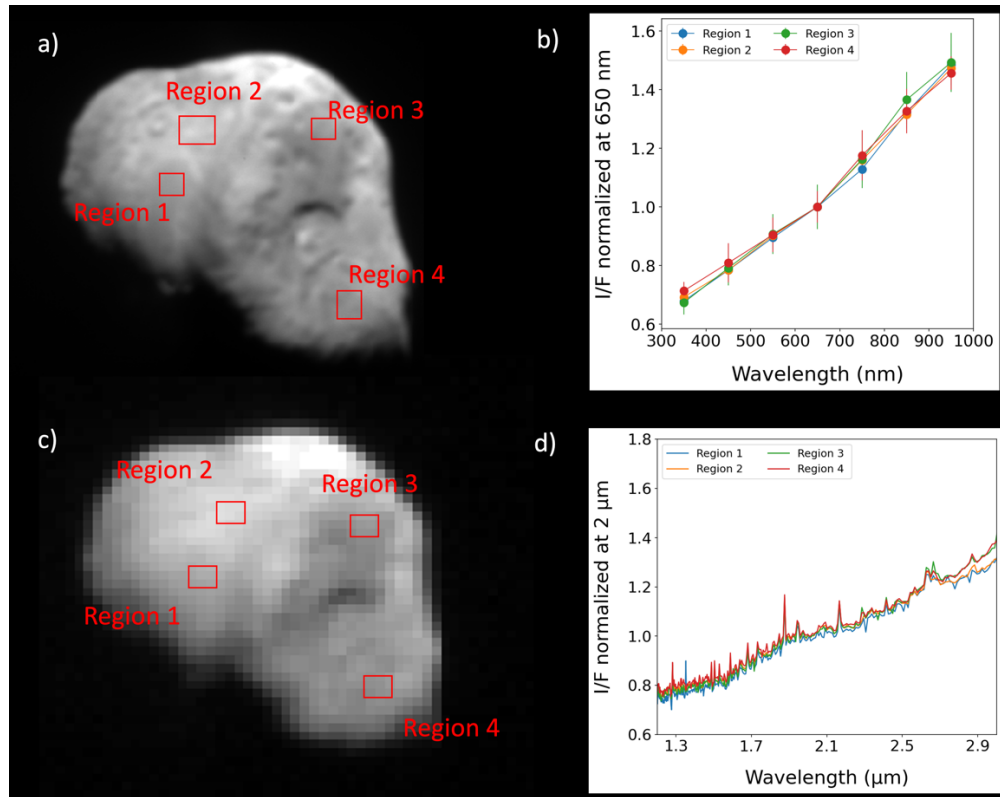


Fig. 4. a) HRI image showing the four regions (red squares) from which we take spectra (b) by means of the color filters. c) IR reconstructed image showing the regions (red squares) from which the IR spectra (d) are taken. Region 1 corresponds to the large smooth patch in both images. In no case, there are differences with the rest of the surface.

3.2 Spatial Measurements from Image Data

First, we took measurements after projecting the images onto the updated shape model. Since the shape model captures the elevation of the cliff that borders the large smooth patch, we selected points on both sides and obtained the relative height of points 0-16 (pairs a-b, one in the inner lower region and the other in the outer higher region), as shown in image 5a. To do this, we used the Small Bodies Mapping Tool software (SBMT²). Because this body is not a spheroid, we cannot simply use the radius differences of each pair as height. Instead, we project the shorter vector onto the longer one, obtaining an average height of this edge of 0.054 ± 0.017 km. Additionally, we used SBMT to draw polygonal lines on the edges of the cliff and the smooth patch (Fig. 5b), which yielded areas of 7.14 and 1.72 km², respectively. Note that it is not always possible to precisely determine the boundaries that define the edge of the cliff or the large smooth patch, and shadows in certain regions also complicate this task. Therefore, these area measurements are approximate and should be used cautiously, as an indication of the order of magnitude of the extent of both regions.

² <https://sbmt.jhuapl.edu/>

To measure the thickness of the smooth patch, we applied the method described in Section 2.2 to ITS images (Fig 2a), measuring the emission angle and the projected edge length in several sections, estimating a thickness of 0.025 ± 0.005 km.

Based on these measurements, we calculate volumes for both the large smooth patch and the cliff region, yielding ~ 0.04 and ~ 0.38 km³, respectively. Given that spectral data indicates the smooth patch shares a similar composition with the surrounding surface, assuming a uniform density —400 kg/m³, [Richardson et al., \(2017\)](#)— allows us to estimate a mass of 1.72×10^{10} kg for the smooth patch. Additionally, if we consider the entire cliff region to be filled, the total mass rises to 15.4×10^{10} kg, representing an order of magnitude increase (see Table 1).

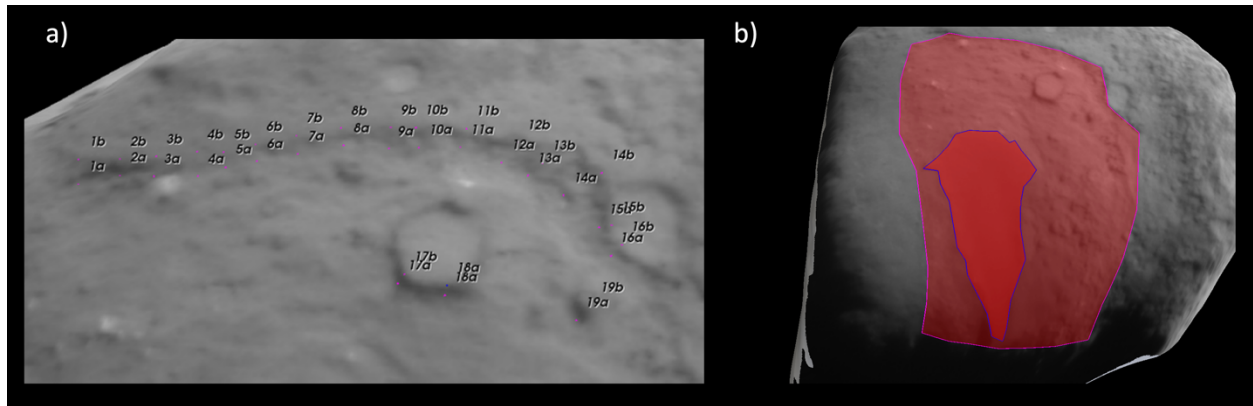


Fig. 5. a) Example of measurements of cliff region and the smooth patch area using the SBMT software. a) Pairs of points used to measure elevations using the shape model. b) Area measurements after projecting images onto the shape model. The cliff region we provide values for is the area between the dark red zone and the light red zone.

Table 1. Obtained values for the area, thickness, and volume of the smooth patch and the cliff region. The calculated mass is obtained using a density of 400 kg/m³.

	Large smooth patch	Cliff region
Area (km ²)	1.72	7.14
Thickness (km)	0.025	0.054
Volume (km ³)	0.04	0.38
Mass (kg x 10 ¹⁰)	1.72	15.4

To explore the large smooth patch morphology, we created anaglyphs (Fig. 6) using three pairs of ITS, HRI, MRI, and SDN images that exhibit suitable changes in viewing geometry. Fig. 6a is composed of the 5070405_9000639 ITS image (cyan) and the deconvolved 9000904 HRI image (red). Fig. 6b is composed of 30034 (cyan) and 30035 (red) SDN images. Post-impact Fig. 6c is composed of MRI images, 5070405_9000999 (cyan) and 5070405_9001012 (red). The three-dimensional view confirms that the central region of the smooth patch is lower than the sides, forming a U-shape.

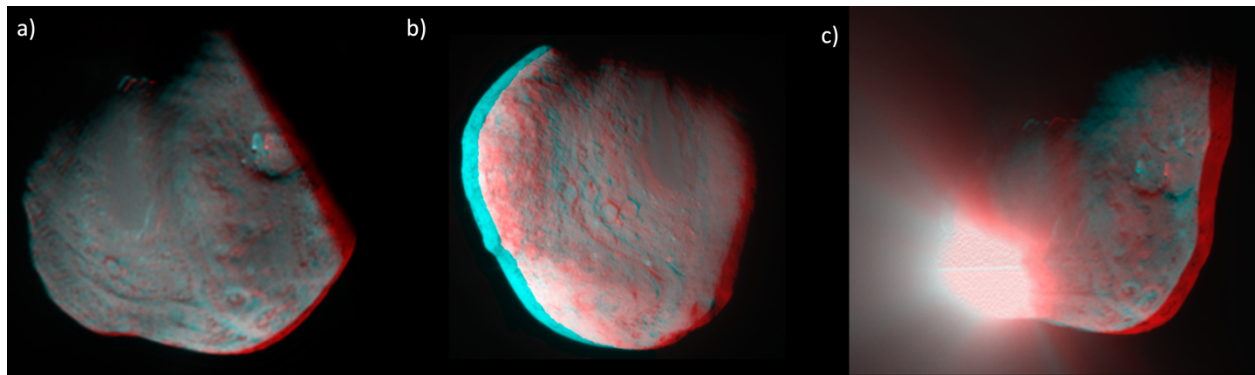


Fig. 6. Anaglyphs to visualize the three-dimensional structure of the large smooth patch. These are composed of: a) cyan ITS image 5070405_9000639 paired with the red deconvolved HRI image 9000904, b) cyan image 30034 combined with red image 30035 from SDN, and c) cyan post-impact 5070405_9000999 overlaid with red image 5070405_9001012, both MRI images. The resultant three-dimensional perspective distinctly illustrates that the central region of the smooth patch dips lower than its surrounding sides, forming a discernible U-shape.

Then, to quantify that lateral elevation, we utilize the shadow lengths observed in NavCam images (refer to Section 2.2). Prior to this, for this shadow method validation, we employed distinct crater control points and features from the shape model (Fig. 5a, pairs 17-19). Through both methodologies, a discrepancy of approximately 10 meters was noted. Then, three parallel lines towards the Sun are drawn on the T1 surface (Fig. 2b). This yields measurements of 0.021 ± 0.001 , 0.018 ± 0.001 , and 0.009 ± 0.001 km for L1, L2, and L3 respectively, indicating an increase in elevation towards the south pole.

3.3 A thorough comparison between Deep Impact and Stardust images

Because DI and SDN acquired images separated by approximately one period, we can study ice sublimation and analyze its evolution on T1. The inspection of both sets of images confirms that there are differences. However, due to differing viewing geometries and camera characteristics such as dynamic range, thermal stability, or spatial resolution, it is not always straightforward to confirm whether these differences are real.

Our approach here is to project the images onto the shape model and blink them. First, we record all apparent differences. Next, we discuss whether these differences are real or false positives based on their location, and morphology and after checking if they are systematic features observed in multiple images. Only the most evident real changes are included in this section, discarding all those variations that are not obvious. As an illustrative example, we show in Fig. 7 the projected 30036 DI and 5070405_9000673 SDN images.

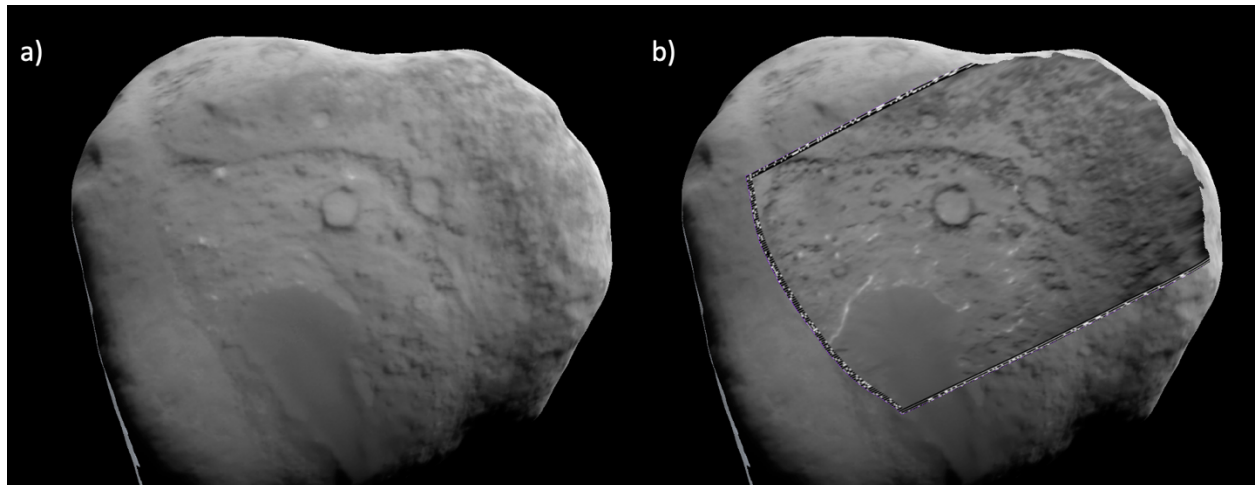


Fig. 7. a) 30036 NavCam image projected onto the T1 shape model. b) Same as (a) but with 5070405_9000673 ITS image overlaid.

In this [link](#), a GIF blinking the images from Figure 7 can be accessed, while this other [link](#) shows the same pair of images with labels. We labeled pairs of bright spots that are present in both DI and SDN images but show an offset as D1-8. We suspect that these bright spots are reflections from ice that shift due to the changes in incidence and emission angles after sublimation modified the morphology of the surface. As P1-12, we also label another group of bright spots that only appear in the DI image but not in the SDN image. If these are reflections, it could be that after ice sublimation, the new incidence and emission angles make them not visible from the position in which the SDN camera was located.

On the other hand, we labeled linear structures that appear in the DI image but not in the SDN image as N1-9, and we indicated edge offsets as L1-9. Finally, we mark regions where sublimation reduced some areas in the large smooth patch as A1-8. The most prominent is A1, a portion of the smooth patch edge that has completely sublimated. It occupies an area of approximately 0.04 km^2 . Since the thickness of this feature is 0.025 km , we can establish a sublimation rate of at least 10^6 m^3 per period.

3.4 Ice-flow simulation

As explained in Section 2.2, we decided to explore the ice flow hypothesis using the new shape model and simulating gravitational flow. To do this, we first created a grid on the T1 surface with a step of 200 km and simulated all possible solutions. All simulations with the seed placed in the southern hemisphere ended up filling the area where the large smooth patch is located due to it being in a gravitational potential well. However, the most interesting solutions appear when we place the seed between $160^\circ < \text{longitude} < 190^\circ$ and $-20^\circ < \text{latitude} < -40^\circ$ (see Fig. 9-2). In this case, the flow not only occupies the area where the large smooth patch is located but also moves along other T1 faces and floods them.

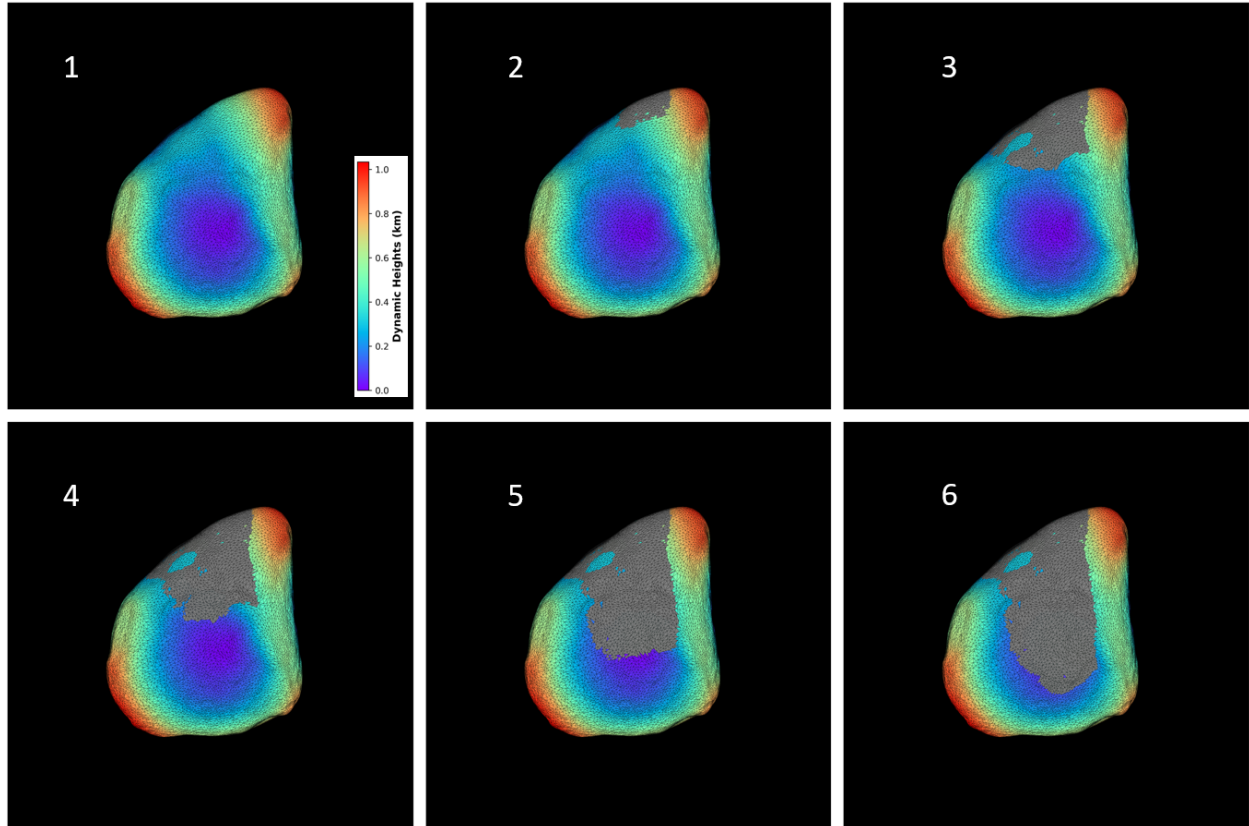


Fig. 9. 1) Initial state of the T1 surface before running the simulation. 2) Starting point: seed located in the region between 160° and 190° longitude and -20° and -40° latitude. Figures 3, 4, 5, and 6 represent the 15th, 30th, 45th, and final steps of the simulation, respectively. The blue-red color scale on the facets represents the gravitational potential value converted to dynamic heights, while the gray facets represent the simulated flow. The shape model has been downsampled to 31,456 facets to reduce computation time.

In Fig. 9, we compare the simulation output with the real images. We see how the secondary smooth patch found adjacent to the crater/pit-like feature would be connected to the largest one assuming a gravitational flow (Fig. 10a). In Fig. 10d, we see how the northern face would also be occupied by this material, precisely close to the area where SDN images captured signs of mass wasting.

Therefore, if this simulation approximately represents what happened, it could explain not only the presence of the large smooth patch but also the secondary one, connecting these features with the

observed hints of mass wasting on the opposite northern face. Thus, it means that a single event triggered an ice flow that moved across the entire surface. In this way, the cliff near the large smooth patch would mark the boundary of the erosion caused by this flow, and the cliff region would be the remnant after the subsequent sublimation.

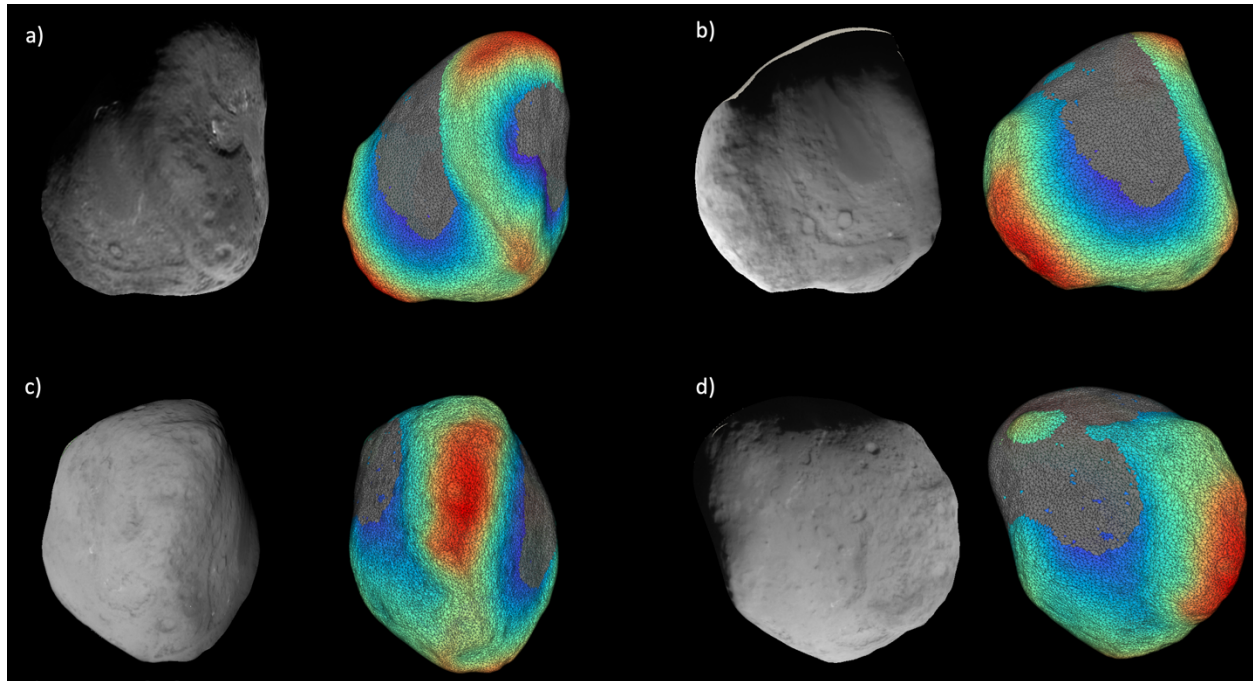


Fig. 10. Same as Fig. 9 but with the shape model reoriented to match the real images for comparison: (a) corresponds to deconvolved 9000909 HRI, while (b), (c) and (d) are 30036, 30037, and 30039 NavCam images, respectively. This simulation connects the large smooth patch, the secondary smooth patch, and the hints of mass wasting on the opposite northern face because of a single event.

3.5 Modeling solar and thermal self-irradiation

As described in Section 2.2 we compute the incoming solar radiation received by T1 in a complete orbit together with the shadowing and self-heating effects using a ray-tracing algorithm.

The results of this calculation are shown alongside DI images (Fig. 8a) and SDN images (Fig. 8b, c, d) using the same perspective for comparison. In Figs. 8a and 8b, we see that the area containing the larger smooth patch is the least irradiated, while the irradiation increases by a factor of 3 in the cliff region, i.e., the intermediate area between this feature and the cliff. The red circle indicates another area in the equatorial region that appears to have smooth terrain (hereinafter referred to as the secondary smooth patch), although, unfortunately, there are not more DI or SDN images available from different perspectives to characterize it. The equatorial regions show the highest irradiance (Fig. 8c). The side opposite the large smooth patch (Fig. 8d) has received irradiation similar to that observed in the cliff region. A blue circle highlights a region that shows signs of mass wasting, while the arrows indicate other smooth regions that appear in T1.

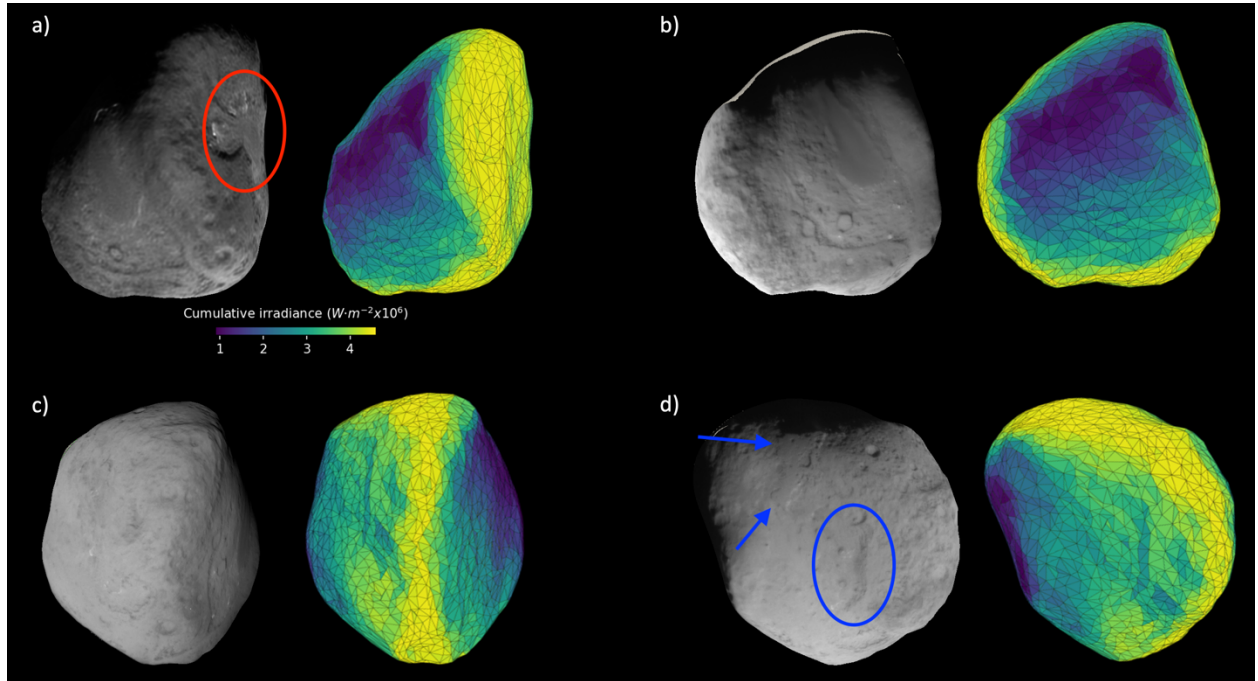


Fig. 8. Total cumulative irradiance after a complete orbit of T1. It ranges from 0.1 to $4.4 \times 10^6 \text{ W/m}^2$. A real image is placed next to each figure to aid in interpretation: (a) corresponds to deconvolved 9000909 HRI, while (b), (c), and (d) are 30036, 30037, and 30039 NavCam images, respectively. The red circle points out to what seems to be another smooth terrain, the blue circle highlights a region that shows signs of mass wasting, and the blue arrows indicate other smooth regions.

3. Discussion

Spectral data suggests that the large smooth patch has the same composition as the rest of the surface, supporting an endogenous nature. From spatial measurements—anaglyphs and direct measurements on images mapped onto the shape model—we conclude that the smooth patch is a protruding area with an approximate thickness of at least 25 meters, embedded in a cliff about 50 meters high. Morphologically, it has a lobate U-shape, with lateral edges higher than the central area (see Fig. A1 in the Appendix). These characteristics resemble a gravitational flow. Furthermore, our ice-flow numerical simulation supports this hypothesis, suggesting a connection with the secondary smooth patch and the remains of mass wasting on the opposite face as part of a single event. After computing the solar and thermal self-irradiation, we also find that the larger smooth area is the least irradiated. Thus, based on this evidence, we support the hypothesis that the smooth patch is the result of a gravitational flow that began in the equatorial near the antimeridian. This mass moved towards the meridian region, causing a drag of the previous surface that, after sublimation, exposes a cliff and a sunken region. However, it raises intriguing questions: what phenomenon triggered this flow, and when did it happen?

To establish a time frame, we decided to first study the time it would take to sublime a mass equivalent to that contained in the cliff region, using existing data in the literature on the water production rate of T1. We must be aware that this is simplistic approximation given that there are elements such as CO, HCN, CH₃OH, CS, or H₂S (Crovisier et al., 2009) which are not considered. The highest value found is $9.40 \pm 0.69 \times 10^{27}$ molecules/s (DiSanti et al., 2007), while the lowest value was determined by Feaga et al., (2007) at the time of the Deep Impact flyby, at 4.6×10^{27} molecules/s. By using this lower value it is possible to establish a lower boundary. Given that the cliff region occupies 5.95% of the total surface area (7.14 km² out of 119 km²), and assuming a constant and homogeneous water production rate, we estimate that approximately 600 years are needed to sublime the cliff region.

Another method to calculate this more precisely is to focus on the local region and use the sublimation rate determined through morphological variations between the visits of DI and SDN. Considering that the lower sublimation rate identified in our image comparison is ~ 0.04 km²/period, and that the cliff region is ~ 7.14 km², assuming this rate as constant implies that the sublimation must have occurred <1000 years ago. Aware that these are approximate estimates, the temporal boundaries allow us to conclude that this event took place between ~ 600 and ~ 1000 years ago.

Regarding the question of what type of phenomenon triggered this flow, we consider several scenarios. A cryovolcano, which consist of the eruption of liquid or vapor phases of water or other volatiles that would freeze solid on the surface, is a phenomenon compatible with an ice flow, and they have been proposed to explain certain geological features and physical properties identified on several bodies in the solar system. For example, similar nature objects to T1 in the Kuiper Belt, such as Charon or Quaoar (Cook et al., 2007; Jewitt & Luu 2004) has been suggested to present cryovolcanoes. However, the mechanisms that give rise to these events are still not well understood. What is clear is that even at such distant distances from the Sun, there must be energy sources to cause them. For example, the detection of crystalline ice on Quaoar indicates that the temperature has exceeded the critical range for crystallization. The primary assumed sources of energy are either tidal or radiogenic heat. However, for comets, the radioactive decay of short-lived isotopes is considered inefficient. For instance, Choi et al., (2002) demonstrate that in most cases, this decay could only achieve temperatures as low as -93°C as a result of ²⁶Al decay and localized in the nucleus. On the other hand, tidal heating in large bodies is a result of synchronous rotation and is proportional to the satellite radius. Therefore, any analogy with our case is not meaningful.

In comets, we currently know of only two possible energy sources that could fuel a phenomenon of this nature: an impact, or gravitational stresses induced by close proximity to Jupiter. The impact hypothesis is unlikely because comet parent bodies are believed to have formed in low-density regions during the early stages of the solar system, resulting in significantly fewer collisions and, consequently, much lower impact energy for heating (Davidsson et al., 2016). Even in dense regions of the main belt, for bodies ranging from 1 to 10 km in scale, collisional timescales are measured from hundreds to thousands of millions of years (Bottke et al., 2005).

On the other hand, according to Yeomans et al., (2005), comet T1 has undergone dramatic orbital changes due to close approaches to Jupiter over the last few hundred years. The orbit ranged from a perihelion of ~ 1.5 to ~ 3.5 AU, and inclinations from ~ 3 to >15 degrees. Similarly, Ip et al., (2016) performed backward orbital integration for T1 over 1000 years, finding that T1 experienced abrupt changes in its orbit caused by encounters with Jupiter, with a perihelion ranging from 1.4 to 4 AU. These changes would have created

internal tensions due to tidal forces and varying degrees of perihelion heating. As demonstrated by the comet D/Shoemaker-Levy 9 in 1994 ([Asphaug & Benz 1994](#)), the gravitational stresses caused by close proximity to Jupiter are strong enough to induce even tidal breakup events. Moreover, Jupiter encounters are not the only stress mechanisms that comets experience. For example, comets can split (*splitting comets*) without obvious provocation, due to an unknown mechanism ([Sekanina 1997](#)). These events are not currently understood, but one hypothesis suggests that torques generated by the asymmetric loss of mass may alter the spin period, driving comets towards rotational instability and potentially leading to the destruction of the nucleus ([Jewitt 2004](#)). Therefore, although we are still far from understanding all the processes that comets undergo, there are justified reasons to consider that some of these abrupt episodes could result in significant increases in internal pressure and temperature, potentially leading to a cryovolcano-like event.

Another idea involves the possibility of a phase change in an inner layer of T1. On the surface, the absence of atmospheric pressure makes the existence of a liquid phase impossible, but what if non-solid phases of cometary material had existed temporarily in the past? The melting of inner ice, or simply an increase in temperature and/or pressure sufficient to change viscosity or friction coefficient, could cause displacement and drag of materials, which in turn, due to heating by friction, could acquire sufficient viscosity to be reaccumulated in a semi-fluid state.

[De Almeida et al., \(2016\)](#), in their studies of observed outbursts in comet 17P/Holmes, proposed that after an initial heating phase and the sublimation of water ice to form water vapor, some of this vapor could refreeze before escaping. This would block pore space and increase the comet's tensile strength in or near the outer crust region, preventing the release of newly liberated subsurface volatile gases, which would ultimately be discharged in explosive episodes. Such a model could account for the sudden explosive outburst activity observed before and after perihelion. They estimate that internal gas pressures on the order of 1 kPa are necessary to rupture the icy crust, while [Reach et al., \(2010\)](#) estimated that such explosions require tensile strengths on length scales greater than 10 meters to be between 10 kPa and 200 kPa. In addition, according to numerical simulations conducted by [Priainik & Bar-Nun \(1990\)](#), assuming a 10% presence of CO, pressures of up to 2 MPa could be reached when gases sublime within the top 20 meters of depth. Moreover, the pressure must exceed the triple point of water, (611 Pa at 0°C), for pure water, but for impure water, such as saline or with impurities, the requirements for freezing point effects are lower. If something like this occurred, the temperatures and pressures generated readily surpass the triple point requirements, and it could have allowed the upper ice mass to move in the direction of the gravitational gradient. But as with the cryovolcano hypothesis, we need more data, and there is no evidence to date beyond speculation that can support these ideas.

The most studied comet at present is 67P/Churyumov-Gerasimenko (67P). For this comet, there is evidence of a fallback process ([Jindal et al., 2022](#)) that explains the smooth terrains found in the northern hemisphere ([Birch et al., 2017](#)). The obliquity and eccentricity of 67P's orbit result in more particles being released from the nucleus during the southern summer ([Thomas et al., 2015](#)). These particles follow ballistic trajectories, with a significant fraction of centimeter-sized or larger particles eventually falling back to the surface. They accumulate in the cold, gravitational lows of the northern (winter) hemisphere, forming the smooth terrains that evolve on short timescales. [Jindal et al., 2022](#) found that the Imhotep region presents a triple-scarp system, showing very evident changes over short timescales (weeks and months).

To test if this idea is consistent with our smooth terrains, we applied the dust fallback simulation developed for comet 67P (Kloos et al., 2024) to T1. The results are shown in Fig. 9. We see a net accumulation of particles in the face where the large smooth patch is located, and a subtle accumulation of material in the secondary smooth patch. However, on the adjacent face it does not coincide with the remains of mass wasting (Fig. 9d). Furthermore, locally we do not observe a clear correlation between the larger smooth patch and the accumulation of dust. Moreover, we do not understand how the deposition of material could account for erosion to form a cliff like the one observed in T1. Unfortunately, there are not T1 images with the same continuous coverage over time of 67P to evaluate the similarity of this phenomenon, although we cannot rule out that there is some analogy or even this phenomenon influenced the large smooth patch evolution.

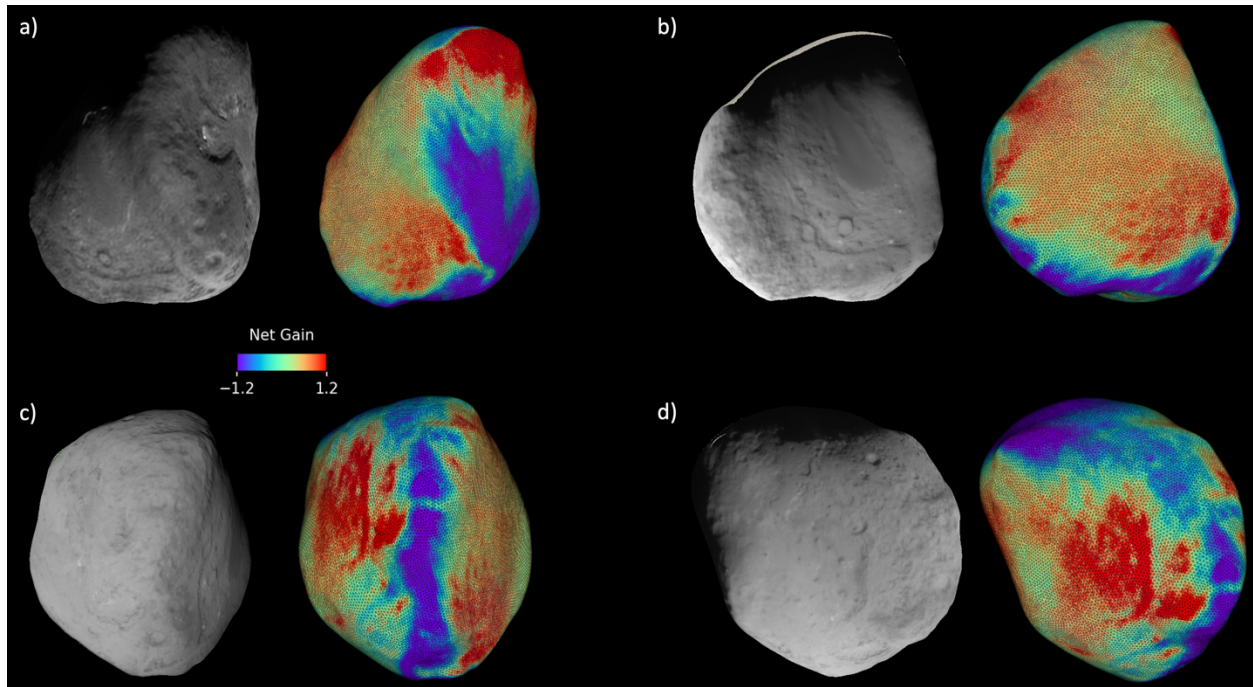


Fig. 9. Net accumulation of dust material across one orbital cycle. A real image is placed next to each figure to aid in interpretation: (a) corresponds to deconvolved 9000909 HRI, while (b), (c), and (d) are 30036, 30037, and 30039 NavCam images, respectively.

In summary, although we have presented and discussed various hypotheses that could explain the origin of this flow, more data is needed to fully understand this phenomenon. Future missions, such as the Comet Interceptor mission (Jones et al., 2024), or The Comet Astrobiology Exploration Sample Return (CAESAR) mission concept (Hayes et al., 2020) could be crucial in providing deeper insights into the evolutionary processes that comets undergo. Future exploring missions will allow us to gather more comprehensive data, enabling a better understanding of the complex mechanisms driving cometary behavior and evolution.

4. Conclusions

In this study, we conducted a detailed analysis of the region containing the large smooth patch to characterize its spectral and morphological features as well as those of its surroundings. Additionally, we developed a series of numerical simulations to calculate solar irradiance and self-heating contributions, testing the viability of it being an ice flow influenced by the gravitational field. Our findings are as follows:

- We determined that the large smooth patch has an approximate thickness of 25 meters and covers an area of 1.72 km².
- The cliff has an average height of ~50 meters, and the intermediate region (cliff region) spans an area of 7.14 km².
- The morphology of the large smooth patch is lobate and U-shaped.
- We observed and characterized significant morphological changes between DI and SDN visits. By measuring changes in the sublimation of the edges of the large smooth patch, we established a sublimation rate of at least 10⁶ m³ per period.
- Gravitational flow simulations suggest that if this phenomenon is responsible, it could explain not only the presence of the large smooth patch but also the secondary one, linking also these features to the observed mass wasting on the opposite northern face. In this case, we interpret the cliff as the drag-induced boundary and the cliff region as the exposed remnant after the sublimation of the missing smooth patch.
- Solar irradiance and self-heating measurements are consistent with the ice flow hypothesis.

Assuming this is an ice flow, we found that this phenomenon occurred between ~600 and ~1000 years ago, and that it was possibly a cryovolcanic process. However, we do not rule out contributions from phenomena such as fallback found on comet 67P, which may have influenced its evolution. Unfortunately, no similar cases have been observed to date, so due to its uniqueness, we must be cautious and await new data to confirm this hypothesis. Future space missions like Comet Interceptor ([Jones et al., 2024](#)) or The Comet Astrobiology Exploration Sample Return (CAESAR) mission concept ([Hayes et al., 2020](#)), will be crucial in providing answers and deepening our understanding of how comets evolve.

Acknowledgments

The authors thank the experts Pedro J. Gutierrez and Jean-Baptiste Vincent for their enriching discussions, Lori Feaga for providing the calibrated spectral data from DI used in this work, and Peter Thomas for providing data for the gravitational numerical simulations. J. L. Rizos acknowledges support from the Ministry of Science and Innovation under the funding of the European Union NextGeneration EU/PRTR.

References

- A'Hearn, M. F., et. al. 2005a. Deep Impact: Working Properties for the Target Nucleus – Comet 9P/Tempel 1. *Space Sci. Rev.* 117, 137–160. <https://doi.org/10.1007/s11214-005-3389-1>
- A'Hearn, M. F., et. al. 2005b. Deep Impact: Excavating Comet Tempel 1. *Science* 310, 258–264. <https://doi.org/10.1126/science.1118923>
- Asphaug, E. & Benz, W. 1994. Density of comet Shoemaker–Levy 9 deduced by modelling breakup of the parent 'rubble pile'. *Nature*, 370, 120–124. <https://doi.org/10.1038/370120a0>
- Bar-Nun, A., et al. 2008. Formation of smooth terrain on Comet Tempel 1. *Icarus* 197, 164–168. <https://doi.org/10.1016/j.icarus.2008.05.007>
- Basilevsky, A. T. & Keller, H. U., 2007. Craters, smooth terrains, flows, and layering on the comet nuclei. *Solar System Research* 41, 109–117. <https://doi.org/10.1134/S0038094607020037>
- Belton, M.J.S., et al., 2007. The internal structure of Jupiter family cometary nuclei from Deep Impact observations: The “talps” or “layered pile” model. *Icarus* 187, 332–344. <https://doi.org/10.1016/j.icarus.2006.09.005>
- Belton, M.J.S., et al., 2009. Fluidization and multiphase transport of particulate cometary material as an explanation of the smooth terrains and repetitive outbursts on 9P/Tempel 1. *Icarus* 200, 280–290. <https://doi.org/10.1016/j.icarus.2008.11.012>
- Belton, M.J.S., et al., 2011. Stardust-NExT, Deep Impact, and the accelerating spin of 9P/Tempel 1. *Icarus* 213, 345–368. <https://doi.org/10.1016/j.icarus.2011.01.006>
- Birch, S. P. D., et al., 2017. Geomorphology of comet 67P/Churyumov–Gerasimenko. *MNRAS*, 469, S50–S67. <https://doi.org/10.1093/mnras/stx1096>
- Bottke Jr, W. F., et al., 2005. Linking the collisional history of the main asteroid belt to its dynamical excitation and depletion. *Icarus*, 179, 63–94. <https://doi.org/10.1016/j.icarus.2005.05.017>
- Chanut, T. G. G., et al., 2015. Mascon gravitation model using a shaped polyhedral source. *MNRAS* 450, 3742–3749. <https://doi.org/10.1093/mnras/stv845>
- Choi, Y.J., et al 2002. Long-term evolution of objects in the Kuiper Belt zone—effects of insolation and radiogenic heating. *Icarus* 160, 300–312. <https://doi.org/10.1006/icar.2002.6976>
- Cook, J. C., et al 2007. Near-Infrared Spectroscopy of Charon: Possible Evidence for Cryovolcanism on Kuiper Belt Objects. *ApJ* 663 1406. <https://doi.org/10.1086/518222>
- Crovisier, J., et al., 2009. The Chemical Composition of 9P/Tempel 1 from Radio Observations. *Eso Astrophysics Symposia*. Springer, Berlin, Heidelberg. https://doi.org/10.1007/978-3-540-76959-0_32
- Davidsson, B.J.R., et al., 2016. The primordial nucleus of comet 67P/Churyumov-Gerasimenko. *Astronomy & Astrophysics* 592, A63. <https://doi.org/10.1051/0004-6361/201526968>

- De Almeida, A. A., et al., 2016. Water outburst activity in Comet 17P/Holmes. *Adv. Space Res.* 58, 444–452. <https://doi.org/10.1016/j.asr.2016.05.001>
- DiSanti, M.A., et al., 2007. Temporal evolution of parent volatiles and dust in Comet 9P/Tempel 1 resulting from the Deep Impact experiment. *Icarus* 187, 240–252. <http://doi.org/10.1016/j.icarus.2006.10.007>
- Duncan, M. J. 2008. Dynamical Origin of Comets and Their Reservoirs. *Space Sci Rev.* 138: 109–126. <https://doi.org/10.1007/s11214-008-9405-5>
- Ernst, C. M., et al., 2019. A Stereophotoclinometry Model of Comet Tempel 1. 50th Lunar and Planetary Science Conference 2019 (LPI Contrib. No. 2132 - 2640)
- Farinella P. & Davis D. R. 1996. Short-period comets: Primordial bodies or collisional fragments? *Science*, 273, 938–941. <https://doi.org/10.1126/science.273.5277.938>
- Farnham, T.L. & Thomas, P.C, 2013. Plate shape model of comet 9p/tempel 1 V2.0, DIF-C-HRIV/ITS/MRI-5-TEMPEL1-SHAPE-MODEL-V2.0, NASA Planetary Data System.
- Feaga, L.M., et al., 2007. Asymmetries in the distribution of H₂O and CO₂ in the inner coma of Comet 9P/Tempel 1 as observed by Deep Impact. *Icarus* 191, 134–145. <http://doi.org/10.1016/j.icarus.2007.04.038>
- Goguen, J. D., et al 2008. Flows on the Nucleus of Comet Tempel 1. *Lunar and Planetary Science XXXIX* - 1969.
- Hayes, A. G., et al. 2020. The Comet Astrobiology Exploration SAmple Return (CAESAR) Mission. American Geophysical Union Fall Meeting.
- Ip, W. H., et al., 2016. Physical properties and dynamical relation of the circular depressions on comet 67P/Churyumov-Gerasimenko. *A&A* 591, A132. <https://doi.org/10.1051/0004-6361/201628156>
- Jewitt & Luu 2004. Crystalline water ice on the Kuiper belt object (50000) Quaoar. *Nature*, 432. <https://doi.org/10.1038/nature03111>
- Jewitt, D. C. 2004. *Comets II*, University of Arizona Press, Tucson, 745 pp., p.659-676
- Jindal, S. A. et al., 2022. Topographically Influenced Evolution of Large-scale Changes in Comet 67P/Churyumov–Gerasimenko’s Imhotep Region. *PSJ*, 3:193. <https://doi.org/10.3847/PSJ/ac7e48>
- Jones, G.H., et al., 2024. The Comet Interceptor Mission. *Space Sci Rev* 220, 9. <https://doi.org/10.1007/s11214-023-01035-0>
- Klaasen, K. P., et al., 2008. Deep Impact instrument calibration. *Review of scientific instruments* 79, 091301. <https://doi.org/10.1063/1.2972112>
- Klaasen, K. P., et al., 2013a. EPOXI instrument calibration. *Icarus* 225, 643–680. <https://doi.org/10.1016/j.icarus.2013.03.024>
- Klaasen, K. P., et al., 2013b. Stardust–NExT NAVCAM calibration and performance. *Icarus* 222, 436–452. <https://doi.org/10.1016/j.icarus.2012.01.025>

Kloos, J., et al., 2014. Investigating Local and Global Scale Dust Redistribution on Comet 67P/C-G. In revision.

Li, J. Y., et al., 2007. Deep Impact photometry of Comet 9P/Tempel 1. *Icarus* 191, 161–175.
<https://doi.org/10.1016/j.icarus.2006.09.027>

Li, J. Y., et al., 2012. Photometry of the nucleus of Comet 9P/Tempel 1 from Stardust-NExT flyby and the implications. *Icarus* 222, 467–476. <https://doi.org/10.1016/j.icarus.2012.02.011>

Lindler, D., et al., 2007. Restoration of images of Comet 9P/Tempel 1 taken with the Deep Impact high resolution imager. *Publ. Astron. Soc. Pacific*. 854, 427-436. <https://doi.org/10.1086/516829>

Prialnik, D. & Bar-Nun, A. 1990. Gas release in Comet Nuclei. *The Astrophysical Journal* 363, 274-282.
<https://doi.org/10.1086/169339>

Reach, W.T., et al., 2010. Explosion of comet 17P/Holmes as revealed by the Spitzer space telescope. *Icarus* 208, 276–292. <https://doi.org/10.1016/j.icarus.2010.01.020>

Richardson, J.E., et al., (2007). A ballistics analysis of the Deep Impact ejecta plume: Determining Comet Tempel 1's gravity, mass, and density. *Icarus* 190, 357–390.
<https://doi.org/10.1016/j.icarus.2007.08.001>

Rickman, H., 2004. Current Questions in Cometary Dynamic. *Comets II*, M. C. Festou, H. U. Keller, and H. A. Weaver (eds.), University of Arizona Press, Tucson, 745 pp., p.205-208.

Sekanina, Z., 1997. The problem of split comets revisited. *Astron. & Astrophys.* 318, L5–L8.

Stern S. A., 1995. Collisional time scales in the Kuiper disk and their implications. *Astron. J.*, 110, 856–868. <https://doi.org/10.1086/117568>

Thomas, N., et al., 2015. Redistribution of particles across the nucleus of comet 67P/Churyumov-Gerasimenko. *A&A*, 583, A17. <https://doi.org/10.1051/0004-6361/201526049>

Thomas, N., et al., 2015. The morphological diversity of comet 67P/Churyumov-Gerasimenko. *Science* 347, 6220. <https://doi.org/10.1126/science.aaa0440>

Thomas, P.C., et al., 1993. Gravity, tides, and topography on Small Satellites and Asteroids: application to surface features of the martian satellites. *Icarus* 105, 326-344. <https://doi.org/10.1006/icar.1993.1130>

Thomas, P.C., et al., 2007. The shape, topography, and geology of Tempel 1 from Deep Impact observations. *Icarus* 187, 4–15. <https://doi.org/10.1016/j.icarus.2006.12.013>

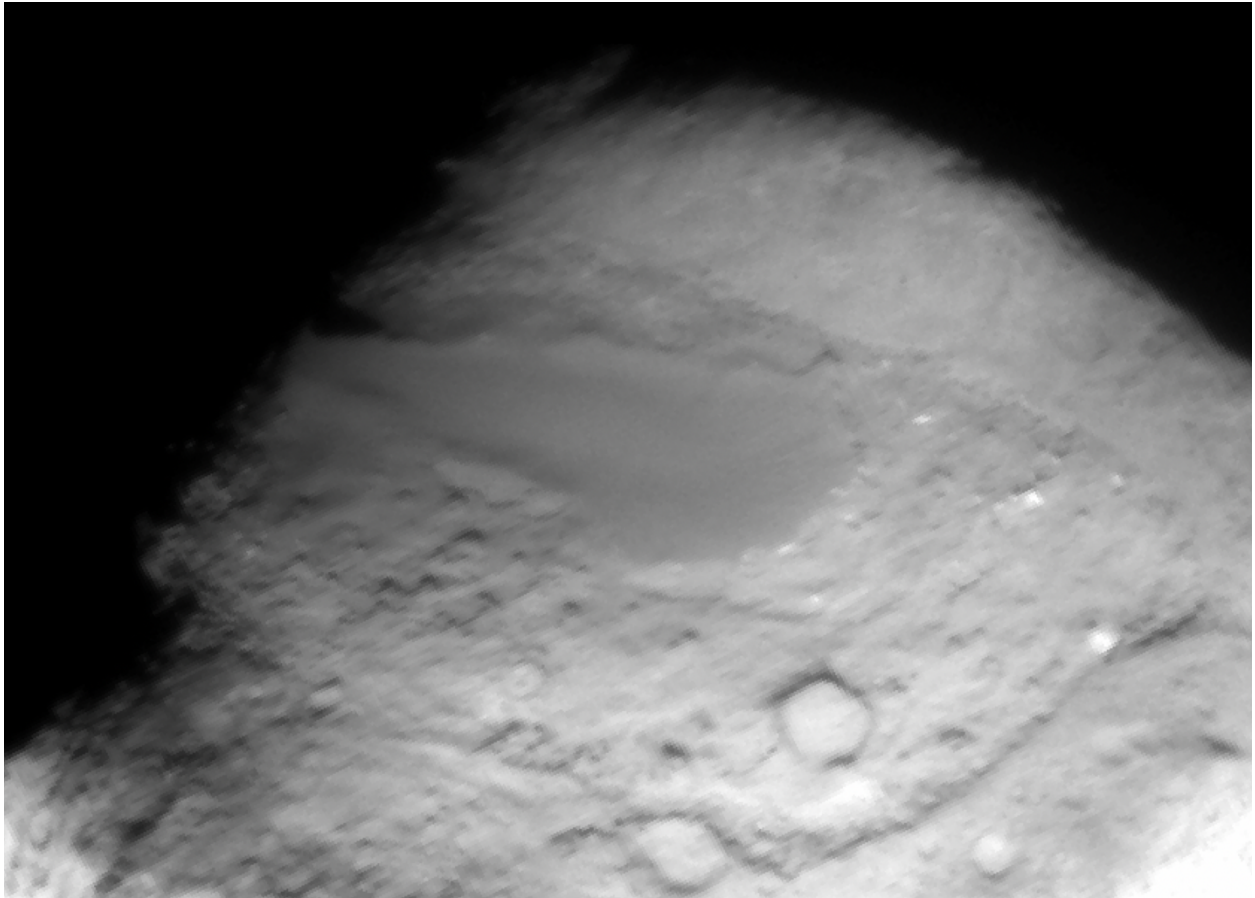
Thomas, P.C., et al., 2013. The nucleus of Comet 9P/Tempel 1: Shape and geology from two flybys. *Icarus* 222, 453–466. <https://doi.org/10.1016/j.icarus.2012.02.037>

Veverka, J., et al., 2013. Return to Comet Tempel 1: Overview of Stardust-NExT results. *Icarus* 222, 424-435. <https://doi.org/10.1016/j.icarus.2012.03.034>

Weidenschilling, S. J., 2004. From icy grains to comets. *Comets II*, M. C. Festou, H. U. Keller, and H. A. Weaver (eds.), University of Arizona Press, Tucson, 745 pp., p.97-104.

Yeomans, D.K., et al., 2005. The History and Dynamics of Comet 9P/Tempel 1. Deep Impact Mission: Looking Beneath the Surface of a Cometary Nucleus. Springer, Dordrecht. https://doi.org/10.1007/1-4020-4163-2_5

Appendix



A1. 30035 SDN image centered in the larger smooth patch. This image shows the three-dimensional morphology of the large smooth patch discussed in the work, its location and context in relation to the exterior cliff, and the rough, pitted terrain on the cliff region located between the cliff and the large smooth patch.